

# On higher-order mixed FEM for low Mach number flows: application to a natural convection benchmark problem

V. Heuveline<sup>\*,†</sup>

*Institute of Applied Mathematics and IWR, University of Heidelberg, INF 293, D-69120 Heidelberg, Germany*

## SUMMARY

We consider higher-order mixed finite elements with continuous pressures for the computation of stationary compressible flows at low Mach number. The proposed approach is based on a fully coupled treatment of the governing equations and therefore, for steady-state calculations, does not rely on time-stepping techniques. The non-linear problem is solved by means of a quasi-Newton iteration. The strongly coupled system resulting from higher-order discretization of the linearized equations requires adequate solvers. We propose a new scheme based on multigrid methods with varying FEM ansatz orders on the grid hierarchy as well as multiplicative smoothers based on blocking techniques. Computational results are described for a benchmark configuration including a flow with heat transfer in the low Mach number regime. Furthermore, the issue of anisotropic grids is addressed in that context. Copyright © 2003 John Wiley & Sons, Ltd.

KEY WORDS: p-FEM; low Mach number flow; multigrid; anisotropic grids; implicit solver

## 1. INTRODUCTION

The higher-order finite-element methods as compared to their lower-order counterpart, provide small diffusion errors, easier implementation of the *inf-sup* condition and an exponential decay of the numerical error for smooth solutions (see Reference [1]). In practice, however, the existence of boundary layers restricts locally the smoothness of the solution and may affect the overall accuracy. Furthermore, the strongly coupled system resulting from higher-order discretization requires suitable solvers.

The goal of this paper is twofold. New solvers based on multigrid methods for higher-order discretization are presented and applied to the simulation of a *thermally driven cavity* in the low Mach number regime. The considered benchmark configuration includes large

---

\* Correspondence to: V. Heuveline, Numerical Analysis, GMP, IWR, University of Heidelberg, INF 293, D-69120 Heidelberg, Germany.

† E-mail: vincent.heuveline@iwr.uni-heidelberg.de

Contract/grant sponsor: BMBF (Bundesministerium für Bildung und Forschung); contract/grant number: RAA1.03M  
Contract/grant sponsor: SFB 359'Reaktive Strömungen, Diffusion und Transport

temperature gradients and is solved for various Rayleigh numbers. The highly non-linear character of the considered equations for this configurations as well as the existence of strong boundary layers imposes the use of an involved solution process. We determine the ‘break-even’ point regarding the order of the discretization and the highest efficiency in order to reach a prescribed tolerance for the Nusselt numbers associated to the two vertical walls of the considered cavity.

The outline of the remainder of this paper is as follow. In Section 2 we formulate the governing equations of the considered low Mach number model and define the benchmark configuration. The discretization of the partial differential equations by higher-order finite element methods is described in Section 3. Section 4 is devoted to the solution process. A quantitative comparison with regard to approximation order and the computational efficiency for the proposed discretizations are presented in Section 5.

## 2. MODEL AND BENCHMARK SPECIFICATIONS

In many flow problems, the velocity of the flow is much slower than the speed of sound. Such low Mach number flows are almost hydrodynamically incompressible and compression is mainly due to thermodynamical effects (e.g. heat transfer). The classical compressible form of the Navier–Stokes equations does not take advantage of this property since this model includes the propagation of acoustic waves. Furthermore, it is well known that the incompressible Navier–Stokes or the Boussinesq equations are valid only under the assumption of small temperature gradients [2]. Several approaches have been developed in order to derive low Mach models from the compressible or incompressible Navier–Stokes equations (see e.g. References [3–11]). A classical approach is based on the decoupling of the density variable from the hydrodynamical pressure (see e.g. Reference [6]). The resulting system of equations reads

$$\partial_t \rho + \nabla \cdot (\rho v) = 0 \quad (1)$$

$$\partial_t(\rho v) + \nabla \cdot \rho v v + \nabla p + \nabla \cdot \tau = \rho g \quad (2)$$

$$c_p \rho D_t T - D_t p - \nabla \cdot (\kappa \nabla T) + (\tau : \nabla v) = 0 \quad (3)$$

$$\rho = \frac{p_{\text{th}}}{RT} \quad (4)$$

where  $D_t f := \partial_t f + v \cdot \nabla f$  describes the substantial time derivative. In the equations of motion (2) and energy (3), the *stress tensor* is denoted by  $\tau$ . We assume Newtonian fluids and neglect the *bulk viscosity* which leads us to the following expression:

$$\tau := \mu(\nabla u + \nabla u^T) + \frac{2}{3}\mu(\nabla \cdot u)I \quad (5)$$

where  $\mu$  is the coefficient of the *shear viscosity*. The shear viscosity is assumed to be constant or to fulfil the *Sutherland law* approximation (see e.g. Reference [12]), i.e.:

$$\mu(T) := \left(\frac{T}{T^*}\right)^{3/2} \left(\frac{T^* + S}{T + S}\right) \mu^* \quad (6)$$

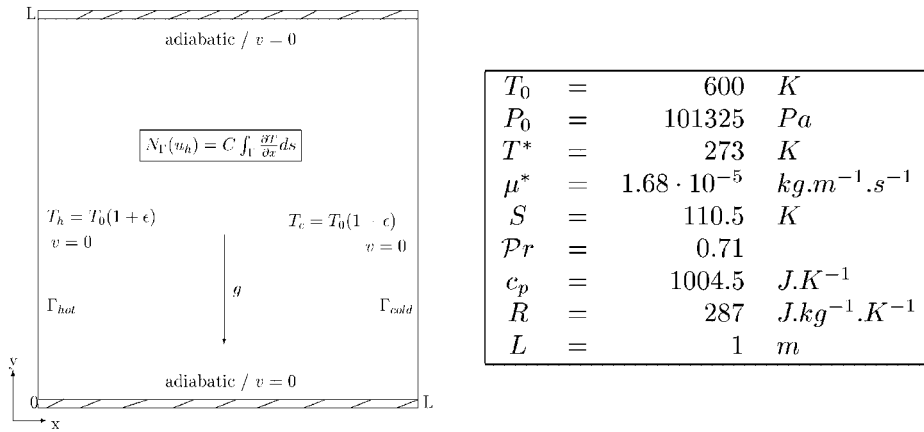


Figure 1. Configuration of thermally driven cavity (left) and corresponding parameters (right).

where  $S$  is the *Sutherland constant*. The coefficient  $c_p$  represents the *specific heat* at constant pressure and is supposed to be constant. The quantity  $\kappa$  is the *thermal conductivity coefficient* and is assumed to have the following form:

$$\kappa(T) := \frac{c_p}{\mathcal{P}r} \mu(T) \tag{7}$$

where  $\mathcal{P}r$  is the *Prandtl number* based on reference transport properties (see Figure 1). The total pressure  $p$  is splitted into two parts

$$p(x, t) = p_{th}(t) + p_{hyd}(x, t) \tag{8}$$

where the *thermodynamical pressure*  $p_{th}$  is constant in space and the *hydrodynamical pressure*  $p_{hyd}$  is neglected in the perfect gas law (4). Since we restrict ourselves to steady-state flows in an enclosure (see Figure 1), the thermodynamical pressure can easily be derived from a mass conservation argument which leads to the following expression:

$$P_{th} = m_0 \left( \int_{\Omega} \frac{1}{RT} dx \right)^{-1} \tag{9}$$

where  $m_0$  describes the initial mass

$$m_0 = \int_{\Omega} \rho_0 dx = \frac{1}{R} \int_{\Omega} \frac{P_0}{T_0} dx \tag{10}$$

for some given reference temperature  $T_0$  and thermodynamic pressure  $P_0$ . In the more general set-up of non-stationary state flows, the thermodynamic pressure is given by an ODE in time (see Reference [11] for more details). Further, the external forces are described by  $g$  and are limited to gravitational forces in our context. Equations (1)–(3) must be supplemented with adequate boundary conditions. This will be done more precisely in the following for the considered benchmark problem.

Le Quere and Paillere [13] have proposed a benchmark problem for natural convection flows with large temperature gradients. It aims at defining reference solutions for various parameter

set-ups in order to be able to compare numerical solvers with regard to performances and accuracy in the lowMach number regime. The benchmark problem is for a buoyancy-driven flow in a two-dimensional square enclosure  $[1, L] \times [1, L]$ . Its configuration consists of two insulated horizontal walls and two vertical walls heated to  $T_h$ , respectively, cooled down to  $T_c$  (see Figure 1). This problem exhibits complex features (see Figure 4) depending on the *Rayleigh number*

$$\mathcal{Ra} = \mathcal{Pr} \frac{g\rho_0^2(T_h - T_c)L^2}{T_0\mu_0^2} \quad (11)$$

and on the temperature difference parameter

$$\varepsilon := \frac{T_h - T_c}{T_h + T_c} \quad (12)$$

In expression (11), the quantities  $\rho_0 = \rho(T_0, P_0)$  and  $\mu_0 = \mu(T_0)$  describe the density and shear viscosity at given reference temperature  $T_0$  and thermodynamic pressure  $P_0$ . The assumed numerical values of the initial conditions as well as of the model's coefficients are given in Figure 1. Further, we assume no-slip boundary conditions for the velocity on the rigid walls. Neumann boundary conditions for the temperature on the horizontal walls ensure their adiabatic properties whereas, on the vertical walls, Dirichlet boundary conditions for the temperature are imposed. The quantities of interest are the heat transfer to the hot and cold wall represented by the local and average *Nusselt* number respectively defined by

$$\mathcal{Nu}(y) = \frac{L}{T_h - T_c} \left( \frac{\kappa(T)}{\kappa(T_0)} \right) \frac{\partial T}{\partial n}, \quad y \in \Gamma \quad (13)$$

$$\langle \mathcal{Nu} \rangle = \frac{1}{L} \int_{y=0}^{y=L} \mathcal{Nu}(y) \, dy \quad (14)$$

where  $\Gamma = \Gamma_c$  (resp.  $\Gamma = \Gamma_h$ ) for the cold (resp. hot) wall.

### 3. DISCRETIZATION

Our approach is based on conforming mixed finite elements discretization with continuous pressure (see References [14, 15]). We first derive a variational formulation of the system of equations (1)–(3). Let  $\Omega \subset \mathcal{R}^d$  describe the computational domain which is assumed, for simplicity, to be polygonal. Let  $(\cdot, \cdot)$  denote the usual  $L^2(\Omega)$  scalar product in  $\Omega$ . The function space  $H^1(\Omega)$  is the classical Sobolev space of  $L^2(\Omega)$ -functions with generalized (in the sense of distributions) first-order derivatives in  $L^2(\Omega)$  and  $H_0^1 := \{u \in H^1(\Omega); \text{trace}(u) = 0\}$ . Further, we denote

$$L_0^2(\Omega) := \left\{ p \in L^2(\Omega); \int_{\Omega} p \, dx = 0 \right\}$$

The variational formulation of the stationary form of system (1)–(3) is obtained by multiplying the equations by appropriate test functions  $\phi := \{\chi, \psi, \pi\}$  and integrating over the domain  $\Omega$ .

This leads us to define the stationary semi-linear form  $a(\cdot; \cdot)$  by

$$\begin{aligned}
 a(u; \phi) := & (-T^{-1}v \cdot \nabla T, \chi) + (\nabla \cdot v, \chi) \\
 & + (\rho(v \cdot \nabla)v, \psi) + (\mu \nabla v, \nabla \psi) + \left( \frac{1}{3} \mu \nabla \cdot v - p, \nabla \psi \right) - (\rho g, \psi) \quad (15)
 \end{aligned}$$

$$- c_p(\rho v \cdot \nabla T, \pi) - (\kappa \nabla T, \nabla \pi) + (v \cdot \nabla p, \pi) - (\tau : \nabla v, \pi) \quad (16)$$

In the diffusive terms, we have used integration by parts. Let  $X := L \times V^d \times V$  the space of test functions where  $L := L^2(\Omega)$  and  $V := H_0^1(\Omega)$ . Then, the weak formulation of system (1)–(3) reads:

Find  $u := \{p, v, T\} \in u_b + X$ , such that

$$a(u, \phi) = 0 \quad \forall \phi \in X \quad (17)$$

whereas  $u_b$  describes the prescribed Dirichlet data on the boundary  $\partial\Omega$  or on part of it. The thermodynamical pressure  $p_{th}$  (resp. the density  $\rho$ ) is given by the algebraic equation (9) (resp. (4)). In the case that Dirichlet conditions are imposed along the entire boundary  $\partial\Omega$  for the velocity, the hydrodynamical pressure is only defined modulo a constant and the corresponding pressure space is then restricted to  $L_0^2(\Omega)$  (see Reference [16] for more details). This is the case for the considered benchmark configuration.

In order to solve (17) numerically by a Galerkin finite elements method, the infinite dimensional space  $X$  is replaced by a finite dimensional FE-space of functions which are piecewise mapped polynomials on a triangulation  $\mathcal{T}_h$ . The considered meshes are supposed to be *shape regular* and geometrically conforming (see Reference [17]). They consist of curvilinear quadrilateral (or hexahedral) elements  $\{K\}$  covering the domain  $\bar{\Omega}$ . For simplicity, we consider only *affine* meshes where each  $K \in \mathcal{T}_h$  is affine equivalent to the reference element  $\hat{K} := (0, 1)^d$  i.e.  $K = F_K(\hat{K})$  with  $F_K$  affine and orientation preserving. The considered trial and test spaces  $X_h \subset X$  consist of continuous, piecewise polynomial vector functions (so-called  $Q_k$  elements) for all unknowns,

$$X_h^{r,s} := \{(p_h, v_h, T_h) \in C(\bar{\Omega})^{1+d+1} / p_h|_K \circ F_K \in Q_s(\hat{K}); v_h|_K \circ F_K, T_h|_K \circ F_K \in Q_r(\hat{K})\} \quad (18)$$

where  $s = 1$  for  $r = 2$  and  $s = r - 2$  for  $r \geq 3$ . Here,  $Q_r(\hat{K})$  is the space of tensor-product polynomials of degree  $r$  on the reference element  $\hat{K}$  i.e.

$$Q_r(\hat{K}) := \text{span}\{x^i y^j z^k : 0 \leq i, j, k \leq r\} \quad (19)$$

where  $k = 0$  when  $d = 2$ . For simplification, we adopt the notation  $X_h$  to describe  $X_h^{r,s}$  if the order of the discretization needs not to be specified. The resulting discrete problem reads

Find  $u_h = \{p_h, v_h, T_h\} \in u_{b,h} + X_h$  such that

$$a(u_h, \phi_h) = 0 \quad \forall \phi_h \in X_h \quad (20)$$

Equation (17) has *saddle-point* structure due the specific coupling of the pressure and the velocity. This is easily seen noticing that Equation (17) includes the Stokes equations. Therefore, the discretization must fulfil the so-called Babuška-Brezzi (BB) condition which

particularly guarantees a stable approximation of the pressure and avoids the occurrence spurious pressure modes (see e.g. Reference [14]). One important advantage related to the choice of  $X_h$  for the discretization is that this condition is automatically fulfilled and does not necessitate any additional stabilization terms. Indeed for  $r=2$ ,  $X_h$  is related to the classical Hood–Taylor element which is known to be stable uniformly in  $h$  (see e.g. Reference [14]). For  $r \geq 3$ ,  $X_h$  is related to the elements  $Q_r/Q_{r-2}$  for which stability (uniformly in  $h$  while the stability constant degrading  $\mathcal{O}(r^{-1/2})$ ) has been proven by Stenberg and Suri [18]. In the case of equal order trial functions for  $v$  and  $p$ , e.g. the popular  $Q_1/Q_1$ -element, the scheme requires additional pressure stabilization terms which generally degrade the overall precision of the solution.

Further, it has been proved that considering the proposed discretization (19) for the Stokes equations, the *inf-sup* constant related to the Babüska–Brezzi condition is independent of arbitrary large aspect ratios and exhibits the same dependence on  $r$  as in the case of isotropically refined meshes. For two-dimensional (resp. three-dimensional) problems these results are proved in References [19, 20] (resp. [21]). This is an important property since it allows the resolution of boundary layers by properly designed anisotropic meshes (see e.g. References [22, 23]). For the special set-up of the considered benchmark, we consider anisotropic geometric mesh refinement towards the four walls since, especially for higher Raleigh numbers, the solution exhibits stiff boundary layer profiles for the velocity and temperature components (see Figure 4). The construction of the considered anisotropic meshes are related to the scheme proposed by Schötzau *et al.* [20] and reads

Let  $\sigma \in (0, 1)$  and  $\mathcal{T}_{n,\sigma}$  be a triangulation of the interval  $I := (0, 1) = \bigcup_{j=1}^{2n+2} I_j$  such that

$$\begin{aligned} x_0 = 0; x_j &= \frac{1}{2} \sigma^{n+1-j} & j = 1, \dots, n+1 \\ x_j &= 1 - x_{2n+2-j} & j = n+2, \dots, 2n+2 \end{aligned}$$

where  $I_j := (x_j, x_{j+1})$ . The considered geometric tensor product mesh  $\Delta_{n,\sigma}^2$  is then given by  $\mathcal{T}_{n,\sigma} \otimes \mathcal{T}_{n,\sigma}$  i.e.

$$\Delta_{n,\sigma}^2 := \{I_j \times I_k : I_j \in \mathcal{T}_{n,\sigma}, I_k \in \mathcal{T}_{n,\sigma}\} \quad (21)$$

The mesh  $\Delta_{3,0.35}^2$  is shown in Figure 2. This scheme allows the construction of anisotropic meshes with arbitrarily large aspect ratios. In practice, however, due to limitations inherent in the solution process (see Section 4) we restrict ourselves to meshes with aspect ratios below 20.

For transport dominated problems the standard Galerkin finite-element methods are known to produce often widely oscillatory solution on coarse grids. First, this may hint to gain a valuable initial approximation by means of *nested iteration* (see e.g. Reference [24]). Secondly, the robustness and efficiency of the used multigrid method for the solution process (see Section 4) may be greatly deteriorated through such erroneous coarse grid corrections. To cope with this problem we therefore stabilized the dominant convection by means of the usual SUPG approach (‘streamline upwinding Galerkin’ [25]). We refer to the paper of Gerdes *et al.* [26] for a complete description in the context of higher-order methods. This technique which we applied on coarse grids only consists in introducing additional least-square terms in the equilibrium equations. In order to formulate the considered approach in short terms, we write the original system (1)–(3) in the compact form  $L(u)u = 0$  with a non-linear operator  $L(\cdot)$ .

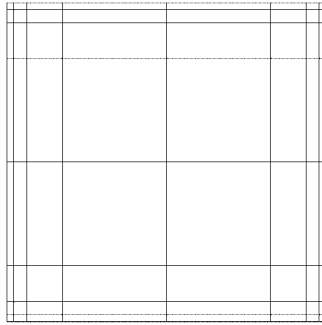


Figure 2. Geometric tensor product mesh  $\Delta_{n,\sigma}^2$  for  $n=3$ ,  $\sigma=0.35$ , aspect ratio = 15.1.

Then, the stabilization process consists in the modification of the original semi-linear form  $a_h, \phi$  by a mesh-dependent semi-linear form

$$a_\delta(u_h, \phi) := a(u_h, \phi) + \langle Lu_h, S\phi \rangle_\delta$$

with a differential operator  $S$  which can be chosen in different ways. Here, we use  $S = -L^*$  and take  $\delta_k \sim h_K$  proportional to the local mesh size,

$$\delta_k = 0.5 \left( \frac{\min\{\mu, \kappa\}}{h_K^2} + \frac{|v|_{\infty, K}}{h_K} \right)^{-1}$$

The  $\delta$ -dependent inner product is defined as usual by

$$\langle u, v \rangle_\delta := \sum_{K \in \mathcal{T}_h} \delta_K(u, v)_K$$

Accordingly, we seek  $u_h \in u_{b,h} + X_h$  such that

$$a_\delta(u_h, \phi_h) = 0 \quad \forall \phi_h \in X_h \quad (22)$$

Regarding the boundary conditions, it is important to notice that the natural boundary conditions for the temperature associated with the weak formulation (15) allow the description of insulated boundaries since they lead to Neumann-type weak boundary condition  $\partial T / \partial n = 0$ . However, this condition is fulfilled in a weak sense only and therefore may not hold pointwise in the discrete space  $X_h$ . This fact, illustrated in Section 5, results physically in imperfectly insulated boundaries. In the context of the considered benchmark this may be a serious drawback for precise calculations since any heat transfer occurring along the walls which are assumed to be insulated may greatly modify the Nusselt numbers associated to the hot and cold vertical walls. As shown in Section 5, the use of higher-order finite elements is a great advantage regarding this issue since they allow to considerably diminish the heat transfer along the insulated boundaries, even on coarse grids.

## 4. SOLVER

In our approach, the non-linear algebraic system (20) is solved implicitly in a fully coupled manner by means of a damped Newton method. Denoting the derivatives of  $a(\cdot, \cdot)$  take at a discrete function  $u_h \in X_h$  by  $a'(u_h, \cdot)(\cdot)$ , the linear system arising at each Newton step  $k$  has the following form:

$$a'(u_h^k, \phi_h)(w_h^k) = (r_h^k, \phi_h) \quad \forall \phi_h \in X_h \quad (23)$$

where  $r_h^k$  is the equation residual of the preceding approximation  $u_h^k$  and  $w_h^k$  corresponds to the needed correction. The updates  $u_h^{k+1} = u_h^k + \alpha^k w_h^k$  with a relaxation parameter by means of Armijo rule are carried out until convergence. On the coarser grids, when the additional transport stabilization terms are included in the discretization (see Equation (22)), the linear system corresponding to (23) reads

$$a'(u_h^k, \phi_h)(w_h^k) + \langle L'(u_h^k)w_h^k, S'(u_h^k)\phi_h \rangle_\delta = (r_h^k, \phi_h) \quad \forall \phi_h \in X_h \quad (24)$$

In practice, the Jacobian involved in (23) (resp. (24)) is directly derived from the analytical derivative of the variational system (20) (resp. (22)).

It is well known that the ability to converge as well as the convergence rate of Newton iterations greatly depend on the quality of the initial approximation (see e.g. Reference [27]). In order to gain such valuable initial approximations, we consider a mesh hierarchy  $\mathcal{T}_h$  with  $\mathcal{T}_{h_l} \subset \mathcal{T}_{h_{l+1}}$  where the corresponding system of Equations (20) are successively solved taking advantage of the previously computed solution i.e. the non-linear Newton steps are embedded in a *nested iteration* process (see Reference [24, chapter 8]). This technique allows in our context to concentrate the needed Newton steps on coarse grids where the resolution of the linear problem (23) remains relatively cheap (see Section 5). In case of transport dominated flows, the stabilized formulation (22) ensures the existence of a solution on such coarse grids.

The linear subproblems (23) (resp. (24)) are solved by the *generalised minimal residual method (GMRES)* (see Reference [28]) preconditioned by means of multigrid iteration (see References [24, 29, 30] and references therein for the description of different multigrid techniques in the context of flow simulation). The proposed preconditioner based on a new multigrid scheme oriented toward conformal higher-order FEM is a key ingredient of the overall solution process and is therefore described in more detail in the following. Two specific features characterize the proposed scheme: varying orders of the FEM ansatz on the mesh hierarchy and Vanka-type smoother [31] adapted to higher-order discretization.

The higher-order discretization results in linear systems which are cellwise and at least componentwise fully coupled. A straightforward application of the multigrid method is not effective since the separation of high- and low-frequency error components on the mesh hierarchy is not possible on such fully coupled patches. Therefore, in our approach, the defect correction on coarser mesh occurs exclusively considering the lowest possible order of our discretization i.e.  $X_h^{2,1}$  related to the Hood–Taylor element. The resulting multigrid scheme can be interpreted as a multiplicative subspace correction [32]. Let  $P_l: X_{h_{l-1}}^{2,1} \rightarrow X_{h_{l-1}}^{r,s}$  describes the interpolation operator between  $X_{h_{l-1}}^{2,1}$  and  $X_{h_l}^{r,s}$  and  $R_l := P_l^*$ . Further, we denote the Jacobian

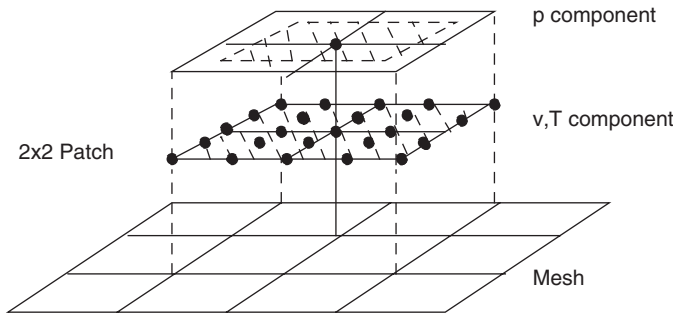


Figure 3. Two-dimensional patch for the smoothing step considering the discretization space  $X_h^{2,1}$ .

defined in Equation (23) (resp. (24)) on level  $l$  by  $A_l$ . The proposed multigrid scheme reads:

- Algorithm 1:**  $u_l^{m+1} = MG(l, r, s, \gamma, u_l^m, f_l, v_1, v_2)$
- (0) **Set discretization space:**  $A_l : X_{h_l}^{r,s} \rightarrow X_{h_l}^{r,s};$
  - (1) **Coarsest grid:** if  $(l=0)$   $u_l^{m+1} = A_l^{-1} f_l;$  return;
  - (2) **Pre-smoothing:**  $\tilde{u}_l^m = S_l^{v_1}(u_l^m)$
  - (3) **Coarse grid correction:**
    - Compute the defect:  $\bar{d}_l^m = f_l - A_l \tilde{u}_l^m;$
    - Restrict the defect in  $X_{h_{l-1}}^{2,1}$   $\bar{d}_{l-1}^m = R_l \bar{d}_l^m;$
    - Recursion:  $\hat{u}_{l-1}^m = MG^{\gamma}(l-1, \mathbf{2}, \mathbf{1}, \gamma, \mathbf{0}, \bar{d}_{l-1}^m, v_1, v_2);$
    - Interpolate:  $\hat{u}_l^m = P_l \hat{u}_{l-1}^m;$
    - Update:  $\tilde{u}_l^m = \tilde{u}_l^m + \hat{u}_l^m;$
  - (4) **Post-smoothing:**  $u_l^{m+1} = S_l^{v_2}(\tilde{u}_l^m)$

Clearly, the coarse grid defect correction in the space  $X_h^{2,1}$  (see Algorithm 1) cannot damp the error components related to the cells inner nodes (see Reference [33]). The proposed smoothing steps consist of multiplicative steps including the solution of local problems on  $2 \times 2$  (resp.  $2 \times 2 \times 2$ ) cell patches for two-dimensional (resp. three-dimensional) problems. On each patch, all velocity and temperature components are included whereas for the pressure components, the inner nodes only are part of the considered local block (see Figure 3). Let  $A_{loc}^p$  describe the Jacobian's block corresponding to the previously mentioned pressure, velocity and temperature components on a given patch  $\mathcal{P}_{2 \times 2}^p$ . Further, for a vector  $w$  we denote by  $w_{loc}$  the local vector containing the  $p$ ,  $v$  and  $T$  components on the current patch. Then, the

smoothing step reads

**Algorithm 2:**  $u^{k+1} = \text{Smooth}(u^k, f)$

**(0) Initialization:**  $\bar{u}^k = u^k;$

**(1) Loop** on the vertices  $\mathcal{V}_p$  of the current mesh  $\mathcal{T}_h;$

**(2) Current patch:** Define the current  $2 \times 2$  patch  $\mathcal{P}_{2 \times 2}^p$  centred on  $\mathcal{V}_p;$

**(3) Compute defect:**  $d_{\text{loc}}^k = (f - A_h \bar{u}^k)_{\text{loc}};$

**(4) Direct Solver:**  $\hat{u}_{\text{loc}}^k = (A_{\text{loc}}^p)^{-1} d_{\text{loc}}^k$

**(5) Update:**  $\bar{u}_{\text{loc}}^k = \bar{u}_{\text{loc}}^k + \omega \hat{u}_{\text{loc}}^k$

**End Loop 1/;**

**(6) Exit:** Set  $u^{k+1} = \bar{u}^k.$

The proposed scheme which is related to the symmetrical coupled Gauss–Seidel (SCGS) method proposed by Vanka [31], is empirically observed to provide good smoothing rates (see Section 5). Similar approaches for the incompressible Navier–Stokes equations considering different discretizations have been proposed by Volker and Tobiska [34]. The solution of the local system in step (4) of Algorithm 2 occurs by means of a direct solver. Two possible computational modii are used in practice. A so-called *resident modus* stores the inverse of the local block  $A_{\text{loc}}^p$  during the overall solution process of the linear system. It allows to increase the numbers  $\nu_1$  and  $\nu_2$  of smoothing iterations with few additional CPU costs. The second *on the fly* modus which is used especially on the finest grids does not store the inverse or any decomposition of local matrices i.e. the local linear subproblems must be solved at each iteration. This modus is clearly much more CPU expensive but relies on minimal memory capacity.

## 5. NUMERICAL RESULTS

In order to investigate the solver performances and the higher-order discretization, we consider four different configurations of the benchmark problem described in Section 2. They differ through the definition of the triplet  $(Ra, \varepsilon, \mu - law)$  whereas  $Ra$  describes the Rayleigh number (see Definition (11)),  $\varepsilon$  is the temperature difference parameter defined in (12) and  $\mu - law$  describes the dependency law of the shear viscosity with regard to the temperature which is assumed in our numerical tests to be constant or to follow the Sutherland approximation (6). The following set-up leads to problems with increasing complexity (see Figures 4 and 5):

If not explicitly mentioned, the coarse grid for the numerical tests is assumed to be  $\Delta_{3,0.35}^2$  defined in (21) and plotted in Figure 2. Due to solver limitations with regard to the aspect ratios, refinement occurs by means of isotropic bisection which leads to embedded finite spaces on the grid hierarchy. Beside the computation of reference solutions for the four cases described in Table I, we compare the approximation capabilities of the different

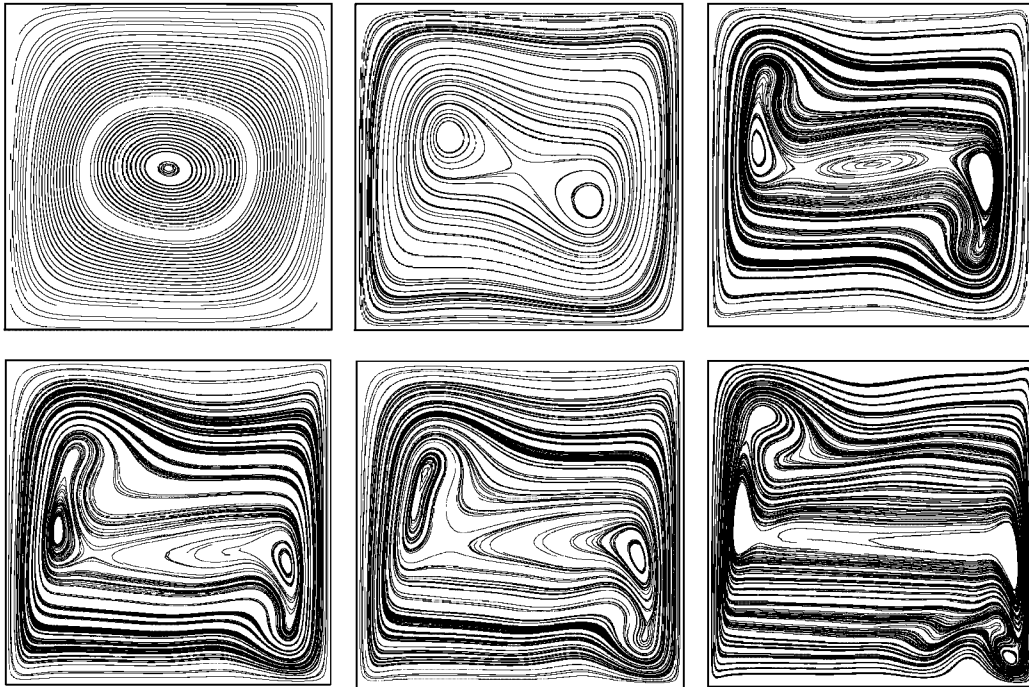


Figure 4. From left to right, top to bottom: streamlines of the heat driven flow for the following triplet  $(Ra, \varepsilon, \mu(T) - law)$ :  $(10^4, 0.01, constant)$ ,  $(10^5, 0.01, constant)$ ,  $(10^6, 0.01, constant)$ ,  $(10^6, 0.6, constant)$ ,  $(10^6, 0.6, Sutherland)$  and  $(10^7, 0.6, Sutherland)$ .

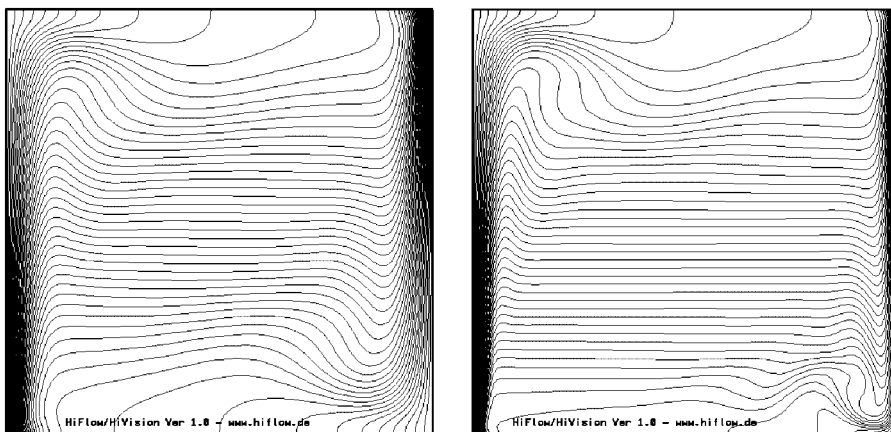


Figure 5. Isolines of the temperature for the experiments  $\mathcal{E}_1$  and  $\mathcal{E}_4$ .

Table I. Benchmark configurations considered for the numerical tests.

Experiment/notation	Rayleigh	$\varepsilon$	$\mu(T) - law$
Exp. 1/( $\mathcal{E}_1$ )	$10^5$	0.01	Constant
Exp. 2/( $\mathcal{E}_2$ )	$10^6$	0.6	Constant
Exp. 3/( $\mathcal{E}_3$ )	$10^6$	0.6	Sutherland
Exp. 4/( $\mathcal{E}_3$ )	$10^7$	0.6	Sutherland

Table II. Convergence records for experiments  $\mathcal{E}_1$  and  $\mathcal{E}_2$  considering the discretization  $X_h^{2,1}$ .

#Dofs	Experiment $\mathcal{E}_1$		Experiment $\mathcal{E}_2$	
	$\langle Nu_{th} \rangle$	$p_{th}/R_0$	$\langle Nu_{th} \rangle$	$p_{th}/R_0$
3556	4.517659	0.9999630227	8.848010	0.8566014202
13 764	4.521599	0.9999630239	8.855156	0.8563334424
54 148	4.521664	0.9999630164	8.859982	0.8563330011
214 788	4.521649	0.9999630161	8.859804	0.8563377658
855 556	4.521649	0.9999630161	8.859780	0.8563378085

Table III. Convergence records for experiments  $\mathcal{E}_3$  and  $\mathcal{E}_4$  considering the discretization  $X_h^{2,1}$ .

#Dofs	Experiment $\mathcal{E}_3$		Experiment $\mathcal{E}_4$	
	$\langle Nu_{th} \rangle$	$p_{th}/R_0$	$\langle Nu_{th} \rangle$	$p_{th}/R_0$
3 556	8.638586	0.920776895	16.387549	0.938574058
13 764	8.683251	0.923645879	16.237860	0.922781637
54 148	8.688562	0.924781637	16.244374	0.922990967
214 788	8.686877	0.924474583	16.242052	0.922821613
855 556	8.686641	0.924447879	16.241706	0.922637156

discretization  $X_h^{r,s}$  defined in (18) for  $r \in [2, 5]$  as well as the efficiency of the proposed solution process.

### 5.1. Toward reference solutions

The quantities of interest are the Nusselt number distribution on the hot and cold walls of the enclosure (see Figure 1), the average Nusselt number and the change of thermodynamical pressure  $p_{th}$  relative to the initial pressure  $R_0$ . The convergence records for the four considered cases (see Table I) considering the discretization  $X_h^{2,1}$  are given in Tables II and III and the corresponding Nusselt number distribution are plotted on Figure 6. It has to be noted that already with  $X_h^{2,1}$  the number of unknowns needed to compute these reference solutions is much lower than their low order (Q1/Q1/Q1 stabilized) counterparts (see References [13, 35, 36]). Beside the fact that the discretization  $X_h^{2,1}$  is stable and therefore do not need additional pressure stabilization terms, the higher-order elements allow to better fulfill

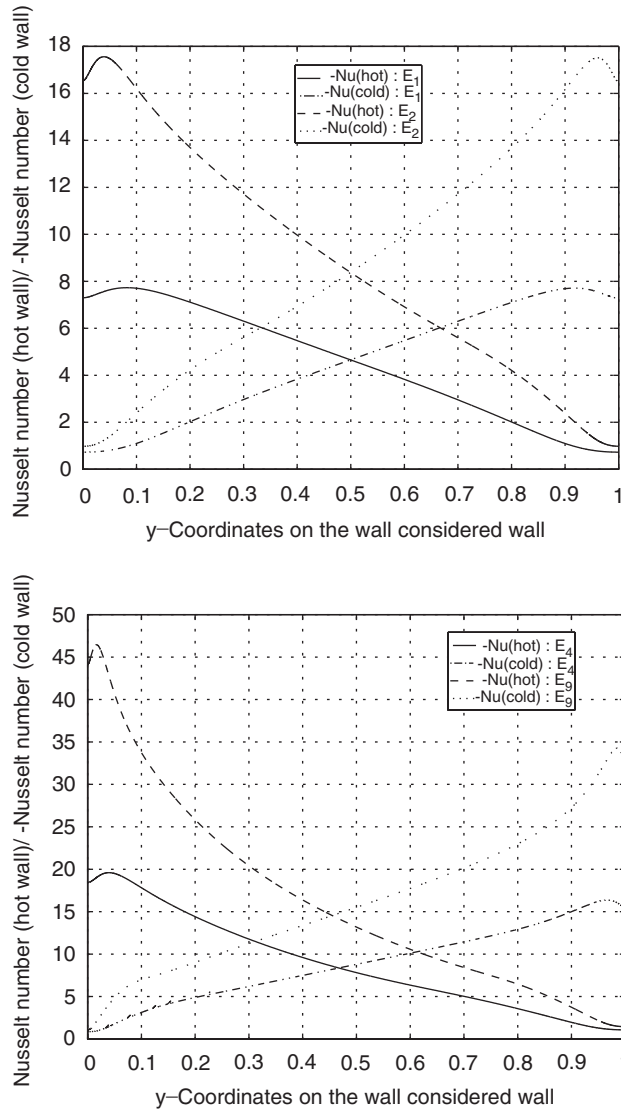


Figure 6. Nusselt number distribution along the hot and cold walls for experiments  $\mathcal{E}_1, \mathcal{E}_2$  (top) and  $\mathcal{E}_3, \mathcal{E}_4$  (bottom).

the physical requirements of adiabatic walls  $\partial T/\partial n=0$  on the top and bottom of the vessel (see Figure 7). Any heat transfer through the top and bottom wall may indeed considerably influence the Nusselt numbers. The resulting reference solutions are summarized in Table IV. For the experiments  $\mathcal{E}_2, \mathcal{E}_3$  and  $\mathcal{E}_4$  the computed solutions are in accordance with the official values given in References [13, 35]. It has to be noted that the dissipative terms ( $\tau:\nabla v$ ) in the energy equation (3) may be neglected for the considered precision of the reference solutions. Assuming perfectly insulated top and bottom walls this leads to  $\langle Nu \rangle_h + \langle Nu \rangle_c = 0$ .

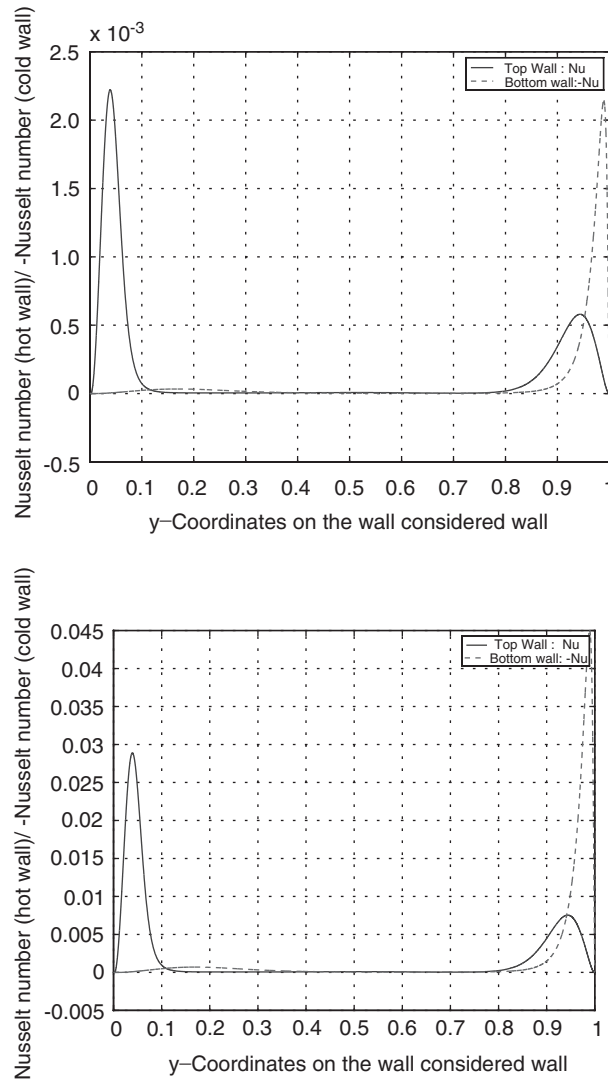


Figure 7. Faulty Nusselt number distribution on the top and bottom walls on the third (resp. fourth) refinement level for experiment  $\mathcal{E}_4$  considering the discretization  $X_h^{2,1}$  (top) (resp.  $Q_1/Q_1/Q_1$  (stabilized) (bottom)).

Further, a repository of reference solutions for a wider range of parameters can be found in Reference [37].

### 5.2. Comparisons between the discretizations

It is well known that for infinitely smooth solutions  $p$ -refinement usually leads to an exponential decay of the discretization error (see References [38, 39] and references therein). The

Table IV. Reference solutions.

Experiment	$\langle Nu_h \rangle$	$p_{th}/R$
$\mathcal{E}_1$	4.521649	0.999963
$\mathcal{E}_2$	8.85978	0.856337
$\mathcal{E}_3$	8.6866	0.9244
$\mathcal{E}_4$	16.241	0.9226

Table V. Comparison of the discretizations in order to reach the Nusselt number on the hot wall with a prescribed tolerance for the relative error of:  $10^{-5}$  for experiment  $\mathcal{E}_1$ ,  $10^{-4}$  for experiment  $\mathcal{E}_2$ ,  $10^{-3}$  for experiment  $\mathcal{E}_3$  and  $10^{-3}$  for experiment  $\mathcal{E}_4$ .

Discretization	# Dofs	Experiments $\mathcal{E}_1$ – $\mathcal{E}_4$				
		# nz entries	$\tau_{disc}^{\mathcal{E}_1}$	$\tau_{disc}^{\mathcal{E}_2}$	$\tau_{disc}^{\mathcal{E}_3}$	$\tau_{disc}^{\mathcal{E}_4}$
$X_h^{2,1}$	54 148	3 024 016	5.7	2.8	1.6	1.3
$X_h^{3,1}$	29 316	2 395 408	4.2	2.1	<u>1</u>	<u>1</u>
$X_h^{4,2}$	13 764	1 654 416	1.3	<u>1</u>	4.3	Divergence
$X_h^{5,3}$	9 668	950 640	<u>1</u>	1.2	8.3	Divergence

goal of this section is to investigate if one can take advantage of this property in the context of flow simulation in the low Mach regime. Especially, the existence of stiff boundary layers profiles deteriorates locally the smoothness of the solution (see Figures 4 and 5). Numerical tests are therefore presented for the four configurations ( $\mathcal{E}_1$ )–( $\mathcal{E}_4$ ) which present decreasing ‘smoothness’ properties. Further, these numerical tests aim at establishing the *break-even* point regarding the order of the discretization and the highest efficiency in order to reach a prescribed tolerance for the needed Nusselt numbers. The performances of each discretization is determined by the CPU time  $t_{disc}^{\mathcal{E}}$  normalized by that of the most efficient alternative  $t_{min}^{\mathcal{E}}$  i.e.

$$\tau_{disc}^{\mathcal{E}} = \frac{t_{disc}^{\mathcal{E}}}{t_{min}^{\mathcal{E}}}$$

The results presented in Table V show the benefit of increasing the order of the discretization with regard to the approximation order. However, for transport dominated problems (cases  $\mathcal{E}_3$  and  $\mathcal{E}_4$ ) the efficiency considering  $X_h^{4,2}$  and  $X_h^{5,3}$  deteriorates greatly. This is mainly connected to the fact that increasing the order of the discretization results in an increase of the number of needed non-linear iterations (see also Section 5.3 as well as Tables VI and VII). Further, each non-linear steps is much more CPU time consuming due the costly integration steps needed to assemble the Jacobians (see Equation 23). Unfortunately, fast quadrature techniques similar to that proposed by Melenk *et al.* [40] cannot be applied for the complex equation set-up inherent to the low Mach model. For the extreme case  $\mathcal{E}_4$  which is at the unsteady limit, the steady state and consequently the convergence could not be achieved for  $X_h^{4,2}$  and  $X_h^{5,3}$ .

Table VI. Records of the reduction factors of the linear and non-linear iterations for the case  $\mathcal{E}_1$ .

# Dofs	$X_h^{2,1}$ (isotropic)		$X_h^{2,1}$ (anisotropic)		$X_h^{4,2}$ (anisotropic)	
	$\rho_{nl}$	$\rho_{lin}$	$\rho_{nl}$	$\rho_{lin}$	$\rho_{nl}$	$\rho_{lin}$
3556	0.13	0.20	0.13	0.21	0.40	0.18
13 764	0.03	0.23	0.03	0.24	0.03	0.20
54 148	0.001	0.28	0.001	0.27	0.01	0.32
214 788	0.001	0.28	0.001	0.28	0.001	0.33
855 556	0.001	0.29	0.001	0.29	0.001	0.34

Table VII. Records of the reduction factors of the linear and non-linear iterations for the case  $\mathcal{E}_3$ .

# Dofs	$X_h^{2,1}$ (isotropic)		$X_h^{2,1}$ (anisotropic)		$X_h^{4,2}$ (anisotropic)	
	$\rho_{nl}$	$\rho_{lin}$	$\rho_{nl}$	$\rho_{lin}$	$\rho_{nl}$	$\rho_{lin}$
3556	0.44	0.28	0.51	0.27	0.64	0.20
13 764	0.21	0.31	0.28	0.34	0.48	0.37
54 148	0.17	0.31	0.17	0.33	0.39	0.37
214 788	0.13	0.32	0.13	0.34	0.31	0.38
855 556	0.06	0.31	0.06	0.35	0.17	0.38

### 5.3. Solver performances

In order to investigate the solver performances, it is applied to the two configurations  $\mathcal{E}_1$  and  $\mathcal{E}_3$ . The multigrid algorithm uses a V-cycle with two pre- and post-smoothing steps i.e.  $\gamma = 1$  and  $\nu_1 = \nu_2 = 2$  in Algorithm 1. The average reduction factor  $\rho_{lin}$  of the linear solver (GMRES preconditioned by means of the multigrid Algorithm 1) is defined by

$$\rho_{lin} = \frac{r_n}{r_0}$$

where  $r_0$  is the initial residual norm on the current grid and  $r_n$  describes the residual norm after the  $n$  linear solver iterations necessitated to fulfil the stopping criteria. Similarly,  $\rho_{nl}$  denotes the average reduction factor of the non-linear steps. In order to analyse the influence of anisotropic grids, comparisons with an isotropic grid which consists in an equidistant tensor product mesh on  $[0, 1] \times [0, 1]$  are given in Table VI (resp. VII) for  $\mathcal{E}_1$  (resp.  $\mathcal{E}_4$ ). The reduction factors of the linear solver show to be almost independent of the mesh size and deteriorate only slightly on the anisotropic grid (aspect ratio  $\tau = 15.1$ ). One observes, however, that the reduction factor of the non-linear iterations becomes worse when increasing the order of the discretization. This implies that the needed number of non-linear steps to achieve convergence increases with the order of the discretization. This constitutes a clear limitation to a pure  $p$ -refinement strategy especially in the context of transport dominated flows generally leading to highly non-linear problems.

## 6. CONCLUSION

For the computation of low Mach number flows, we have described an approach based on a fully coupled treatment of the governing equations. A stable discretization based on higher-order mixed FEM with continuous pressures and a multigrid method including varying order discretizations on the grid hierarchy constitute the two main ingredients of the proposed approach.

The numerical experiments which have been carried out for a natural convection benchmark clearly show the benefit of higher-order discretizations with regard to the approximation order. They further enlighten limitations with regard to the order of the discretization for highly non-linear problems e.g. transport dominated flows. Indeed, for such problems, increasing the order of the FEM ansatz generally results in a considerable increase of the needed non-linear steps. Further, such  $p$ -refinement leads to CPU time-consuming integration steps in order to assemble the Jacobians throughout the non-linear iterations that may greatly deteriorate the overall performances.

The proposed solver shows to be robust for a wide range of problem configurations. The reduction factors of the multigrid methods are almost independent of the mesh size and slightly depends on the aspect ratios  $\tau$  in the range  $\tau \in (1, 20)$ .

## ACKNOWLEDGEMENTS

The author thanks Prof. R. Rannacher for many fruitful discussions. This work was supported by the BMBF (Bundesministerium für Bildung und Forschung) project under grant *RAAI.03M* and the SFB 359 'Reaktive Strömungen, Diffusion und Transport.'

## REFERENCES

1. Babuška I, Suri M. The  $p$  and  $h$ - $p$  versions of the finite element method; basic principles and properties. *SIAM Review* 1994; **36**:578–632.
2. Doering CR, Gibbon JD. *Applied analysis of the Navier–Stokes equations. Cambridge Texts in Applied Mathematics*, CUP: Cambridge, 1995.
3. Bijl H, Wesseling P. A unified method for computing incompressible and compressible flows in boundary-fitted coordinates. *Journal of Computational Physics* 1998; **141**:153–173.
4. De Sampaio PAB, Moreira ML. A new finite element formulation for both compressible and nearly incompressible fluid dynamics. *International Journal for Numerical Methods in Fluids* 2000; **32**:51–78.
5. Bijl H. *Computation of flows at all speeds with a staggered scheme. Ph.D. Thesis*, Technical University Delft, The Netherlands, 1999.
6. Müller B. Computation of compressible low Mach number flow. *Habilitation Thesis*, Swiss Federal Institute of Technology, ETH Zürich, September 1996.
7. Choi Y.-H, Merkle CL. The application of preconditioning in viscous flows. *Journal of Computational Physics* 1993; **105**:207–223.
8. Chen KH, Pletcher RH. Primitive variable, strongly implicit calculation procedure for viscous flows at all speeds. *AIAA Journal* 1991; **29**:1241–1249.
9. Issa RI. Solution of the implicitly discretised fluid flow equations by operator-splitting. *Journal of Computational Physics* 1985; **62**:40–65.
10. Majda A, Sethian J. The derivation and numerical solution of the equations for zero mach number combustion. *Combustion Science and Technology* 1985; **42**:185–205.
11. Majda A. *Compressible Fluid Flow and Systems of Conservation Laws in Several Space Variables*. Applied Mathematical Sciences, Vol. 53, Springer: New-York, 1984.
12. White FM. *Viscous Fluid Flow, 2nd edn*. McGraw-Hill Series in Mechanical Engineering, 1991.
13. Le Quere P, Paillere H. Modelling and simulation of natural flows with large temperature differences: a benchmark problem for low mach number solvers. *Workshop/12th CFD Seminar*, CEA Saclay France, January 2000.

14. Brezzi F, Fortin M. *Mixed and Hybrid Finite Element Methods*, Springer Series in Computational Mathematics, Vol. 15, Springer: New-York, 1991.
15. Nabh G. On higher order methods for the stationary incompressible Navier–Stokes equations. *Ph.D. Thesis*, University Heidelberg, 1998.
16. Heywood JG, Rannacher R, Turek S. Artificial boundaries and flux and pressure conditions for the incompressible Navier–Stokes equations. *International Journal for Numerical Methods in Fluids* 1996; **22**:325–352.
17. Ciarlet PG. *The Finite Element Methods for Elliptic Problems*. North-Holland: Amsterdam, 1978.
18. Stenberg R, Suri M. Mixed hp finite element methods for problems in elasticity and stokes flow. *Numerical Mathematics* 1996; **72**:367–389.
19. Schötzau D, Schwab C. Mixed hp-fem on anisotropic meshes. *Mathematical Methods in Applied Sciences* 1998; **8**:787–820.
20. Schötzau D, Schwab C, Stenberg R. Mixed hp-fem on anisotropic mesh II: Hanging nodes and tensor products of boundary layer mesh. *Numerische Mathematik* 1999; **83**:667–697.
21. Toselli A, Schwab C. Mixed hp-finite element approximations on geometric edge and boundary layer meshes in three dimensions. *Technical Report* 2001-02, Seminar für Angewandte Mathematik, ETH Zürich, February 2001.
22. Dolejsi V. Anisotropic mesh adaptation technique for viscous flow simulation. *East–West Journal of Numerical Mathematics* 2001; **9**(1):1–24.
23. Heuveline V, Rannacher R. A numerical tool for flow simulation in a wankel motor. In *Mathematische Verfahren zur Lösung von Problemstellung in Wirtschaft und Industrie*. Springer: Berlin, to appear.
24. Wesseling P. *An Introduction to Multigrid Methods*. Wiley: Chichester, 1992.
25. Hughes TJR, Brooks AN. Streamline upwind/petrov galerkin formulations for convection dominated flows with particular emphasis on the incompressible Navier–Stokes equation. *Computer Methods in Applied Mechanics and Engineering* 1982; **32**:199–259.
26. Gerdes K, Melenk M, Schötzau D, Schwab C. The hp-version of the streamline diffusion finite element method in two space dimensions. *Technical Report* 1999:35, Chalmers University of Technology and Göteborg University, September 1999.
27. Kelley CT. Iterative methods for linear and nonlinear equations. *Frontiers in Applied Mathematics*, Vol. 16. SIAM: Philadelphia, PA, 1995.
28. Saad Y. Iterative methods for sparse linear systems. *Computer Science/Numerical Methods*. PWS: Boston, MA, 1996.
29. Wesseling P, Oosterlee CW. Geometric multigrid with applications to computational fluid dynamics. *Journal of Computational and Applied Mathematics* 2001; **128**:311–334.
30. Steelant J, Dick E, Pattijn S. Analysis of robust multigrid methods for steady viscous low mach number flows. *Journal of Computational Physics* 1997; **136**:603–628.
31. Vanka S. Block-implicit multigrid calculation of two-dimensional recirculating flows. *Computer Methods in Applied Mechanics and Engineering* 1986; **59**(1):29–48.
32. Xu J. The method of subspace correction. *Journal of Computational and Applied Mathematics* 2001; **128**(1–2):335–362.
33. Hu N, Katz N. Multi-p methods: iterative algorithms for the p-version of the finite element analysis. *SIAM Journal of Science and Computing* 1995; **16**(6):1308–1332.
34. Volker J, Tobiska L. Numerical performance of smoothers in coupled multigrid methods for the parallel solution of the incompressible Navier–Stokes equations. *International Journal for Numerical Methods in Fluids* 2000; **33**(4):453–473.
35. Becker R, Braack M. Solution of a benchmark problem for natural convection at low Mach number. *Technical Report* 30, University Heidelberg, IWR, SFB 359, 2000.
36. Braack M, Rannacher R. Adaptive finite element methods for low-Mach number flow with chemical reactions. In *30th Computational Fluid Dynamics*, N. 1999-03 in Lecture Series. The von Karman Institute, Belgium, 1999.
37. Heuveline V. **HiFlow** a general finite element toolbox for hp-methods. <http://www.hiflow.de>, 2000.
38. Schwab Ch. *p- and hp-Finite Element Methods, Theory and Applications in Solid and Fluid Mechanics*. Oxford Science Publications: Oxford, 1998.
39. Karniadakis G, Sherwin SJ. *Spectrallhp Element Methods for CFD*. Oxford University Press: Oxford, 1999.
40. Melenk JM, Gerdes K, Schwab C. Fully discrete hp-finite elements: fast quadrature. *Technical Report* 1999:52, Chalmers University of Technology and Göteborg University, 1999.